Int. J. Electrochem. Sci., 10 **(2015)** 701 - 712

International Journal of
ELECTROCHEMICAL
SCIENCE
www.electrochemsci.org

Comparative Evaluations on Stress Corrosion Cracking Mechanism of Low Alloy Ultra-High Strength Steels in Neutral 3.5 wt% NaCl Solution

Qiang GUO, Jian-hua LIU[*]*, Mei YU, Song-mei LI*

Key Laboratory of Aerospace Advanced Materials and Performance (Ministry of Education), School of Materials Science and Engineering, Beihang University, Beijing 100191, P. R. China
[*]E-mail: liujh@buaa.edu.cn

Received: 13 October 2014 / *Accepted:* 22 November 2014 / *Published:* 2 December 2014

The stress corrosion cracking (SCC) mechanism of low alloy ultra-high strength steels 30CrMnSiNi2A and 40CrNi2Si2MoVA in neutral 3.5wt% NaCl solution is investigated by slow strain rate technique (SSRT), surface analysis technique and electrochemical measurements. At anodic polarization, 30CrMnSiNi2A shows excellent SCC resistance; on the contrary, 40CrNi2Si2MoVA displays much higher SCC susceptibility than 30CrMnSiNi2A. At cathodic polarization potential, the steels are both susceptible to hydrogen induced cracking (HIC). At OCP, SCC mechanism of 30CrMnSiNi2A is mainly under control of HIC; whereas, SCC process of 40CrNi2Si2MoVA at OCP is controlled by a mixed mode of HIC and anodic dissolution.

Keywords: Stress corrosion cracking; Ultra-high strength steel; Cl^-; HIC; Anodic dissolution

1. INTRODUCTION

In aerospace industry, corrosion problems are inevitable for structural materials in some outstandingly rigorous environment, such as coastal and marine atmosphere environments. For a long time, SCC has been generally acknowledged as a serious problem in marine atmospheric environment for structural metals, particularly for high strength steels [1-4].

Usually, SCC occurs unexpectedly and results in catastrophic accidence. The SCC mechanism of high strength steels is widely accepted as anodic dissolution and HIC [5-6]. The occurrence of SCC behaviour of steels in a certain environment is related with metallurgical microstructure, environmental factors and stress condition [7].

Liu [8] suggested that the SCC mechanism of the high strength steel X70 in the acidic solution was mix-controlled by both anodic dissolution and HIC. Prawoto [9] found that austenite was the most prone to SCC in the different microstructures including austenite, ferrite-pearlite and martensite, respectively. Contreras [10] found that the diffusion of atomic hydrogen was related to the fracture forms, and hydrogen permeation flux increased with the increasing of temperature. Ramamurthy [11] supposed that SCC velocity was independent of steels composition. Saruiglu [12] found that the crack growth behaviour and fracture mode was sensitive to the presence of inclusions and to the microstructure of steels. Hui [13] found that the alloying element Mo could improve the delayed fracture behaviour of high strength steels, and the secondary hardening carbides of V and Mo could also improve the SCC behaviour. Chu [14-15] found that hydrogen could induce delayed plastic deformation and was the necessary and sufficient condition of SCC or hydrogen induced delayed cracking.

30CrMnSiNi2A and 40CrNi2Si2MoVA are two kinds of low alloy ultra-high strength steels, which are widely applied in aerospace and other industries, due to their excellent comprehensive performance, such as ultra-high strength, excellent corrosion resistance, excellent fracture toughness and low manufacturing cost [16-20].

In the present work, SCC behaviour of 30CrMnSiNi2A and 40CrNi2Si2MoVA are comparatively investigated by SSRT with different corrosion potentials, surface analysis technique and electrochemical measurements. It is anticipated that the present research work could provide an essential insight into the SCC mechanism of low alloy ultra-high strength steels in neutral Cl^- environment.

2. EXPERIMENTAL

2.1 Materials and solution

Table 1. The main chemical composition and mechanical properties of 30CrMnSiNi2A and 40CrNi2Si2MoVA

Steel type	C	Ni	Cr	Si	Mn	Mo	V	$\sigma_{0.2}$ / MPa	σ_b /MPa
30CrMnSiNi2A	0.20	1.40	1.20	1.20	1.30	—	—	1450	1800
40CrNi2Si2MoVA	0.40	1.90	0.71	1.66	0.64	0.37	0.088	1640	1980

The main chemical composition and mechanical properties of two kinds of low alloy ultra-high strength steels 30CrMnSiNi2A and 40CrNi2Si2MoVA are shown in Tab.1. The heat treatment system is as follows: 30CrMnSiNi2A was austenitized at 890℃ for 1 h and quenched into oil, then tempered at 280℃ for 2~3 h; 40CrNi2Si2MoVA was austenitized at 870℃ for 1 h, and subsequently quenched in oil, followed by doubly tempering at 300℃ for 2 h with air-cooling to ambient temperature. The steels are machined into flat-plate tensile specimens and the schematic diagrams are shown in Fig.1. The tensile specimens were sealed with epoxy resin without the gauge section. Prior to each SCC test,

the gauge section was ground through successive silicon carbide papers to 800 grits, and subsequently degreased with acetone, washed with deionized water and dehydrated ethanol by an ultrasonic cleaner, respectively, and then dried in air. The experimental solution in the work was neutral 3.5 wt% NaCl solution at room temperature (25±1℃, pH≈6.9).

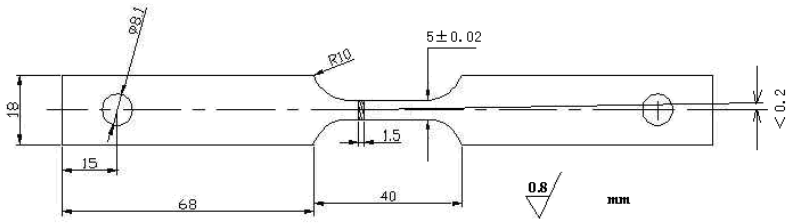

Figure 1. Schematic diagram of the flat plate tensile specimen for 30CrMnSiNi2A and 40CrNi2Si2MoVA

2.2 Slow strain rate test (SSRT)

SSRT was performed on the tensile specimens by a tensile testing system at a strain rate of 1×10^{-6}/s in air and in neutral 3.5 wt% NaCl solution at 25±1℃ with different polarization potentials, such as OCP, –550 mV, –700 mV, –850 mV and –1000 mV with respect to a KCl saturated calomel electrode (SCE). Prior to each test, the specimens were all pre-loaded at 100 N. Each SCC test was repeated at least three times in order to ensure the reliability and accuracy of the experimental data.

2.3 Electrochemical measurements

The electrochemical tests were performed in a conventional 3-electrode cell on a electrochemical working station (VersaSTAT MC-4, Ametek, USA), with a KCl saturated calomel electrode (SCE) as a reference electrode, a grand square platinum plate as counter electrode and the polished steels as the working electrodes. The steel electrodes with exposing area 1 cm^2 were all polished to 2000 grit silicon carbide papers, degreased in acetone, washed in deionized water and dehydrated ethanol before the measurements, respectively. Prior to polarization tests, open circuit potential (OCP) was recorded for at least 1 h until the potential was steady within 10 mV in 10 min. Potentiodynamic polarization curves of the steels were carried out with a potential sweep rate of 0.5 and 50 mV/s.

2.4 Surface characterization

The fracture and the side surface adjacent to the fracture of the SSRT specimens were observed by Field Emission Scanning Electron Microscope (FE-SEM, Apollo 300, CamScan, UK).

3. RESULTS

3.1 SSRT

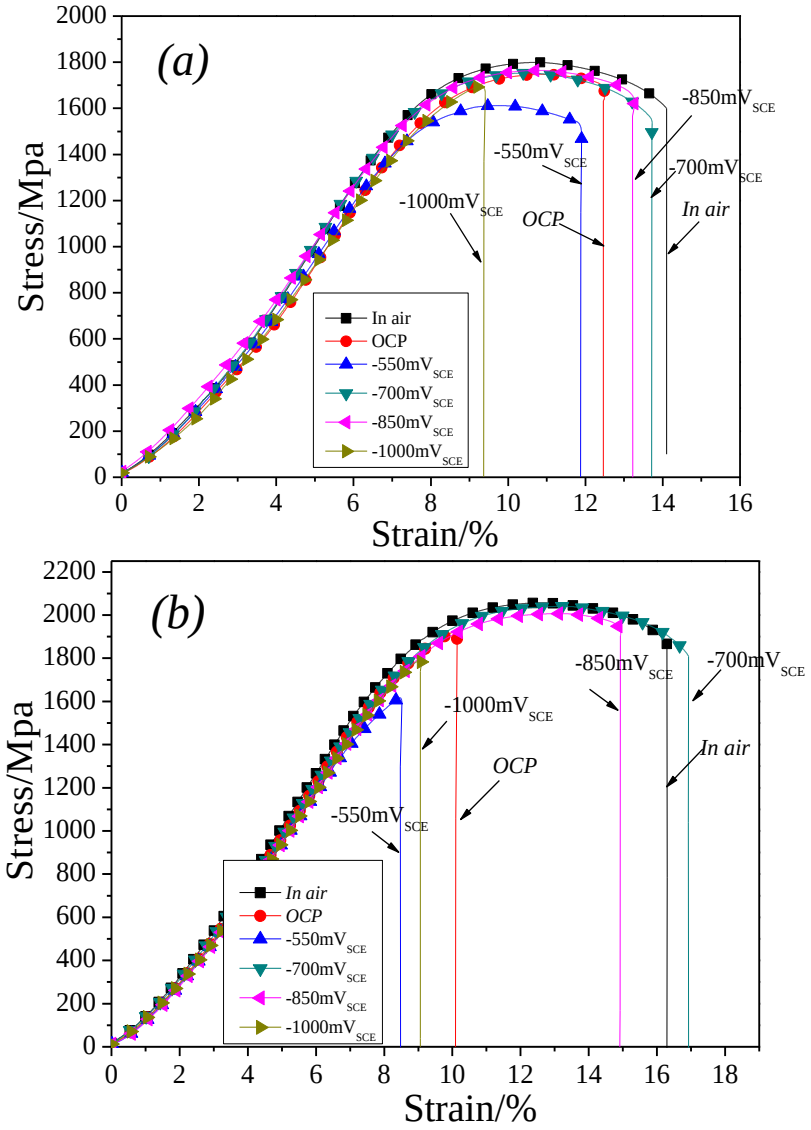

Figure 2. Stress-strain curves of 30CrMnSiNi2A (a) and 40CrNi2Si2MoVA (b) at different polarization potentials in neutral 3.5 wt% NaCl solution

Fig.2 (a-b) are stress-strain curves of the SSRT 30CrMnSiNi2A and 40CrNi2Si2MoVA specimens in neutral 3.5wt% NaCl solution at OCP, –550 mV_{SCE}, –700 mV_{SCE}, –850 mV_{SCE} and –1000 mV_{SCE}, respectively. The specimens tensile in air were selected as the referenced ones in an inert environment without SCC tendency.

The tensile strength loss (I_σ), elongation loss (I_δ) and reduction-in-area loss (I_Ψ) are used to evaluate the SCC susceptibility, which are calculated by Eq. (1-3).

$$\begin{cases} I_\sigma = [1-\frac{\sigma}{\sigma_a}]\times 100 & (1) \\ I_\delta = [1-\frac{\delta_s}{\delta_a}]\times 100 & (2) \\ I_\Psi = [1-\frac{\Psi_s}{\Psi_a}]\times 100 & (3) \end{cases}$$

Where σ_{air}, δ_{air}, and Ψ_{air} are tensile strength, elongation ratio and reduction-in-area ratio of the specimens tensile in air, respectively, and σ_{sol}, δ_{sol}, and Ψ_{sol} are tensile strength, elongation ratio and reduction-in-area ratio of the specimens tensile in neutral 3.5 wt% NaCl solution.

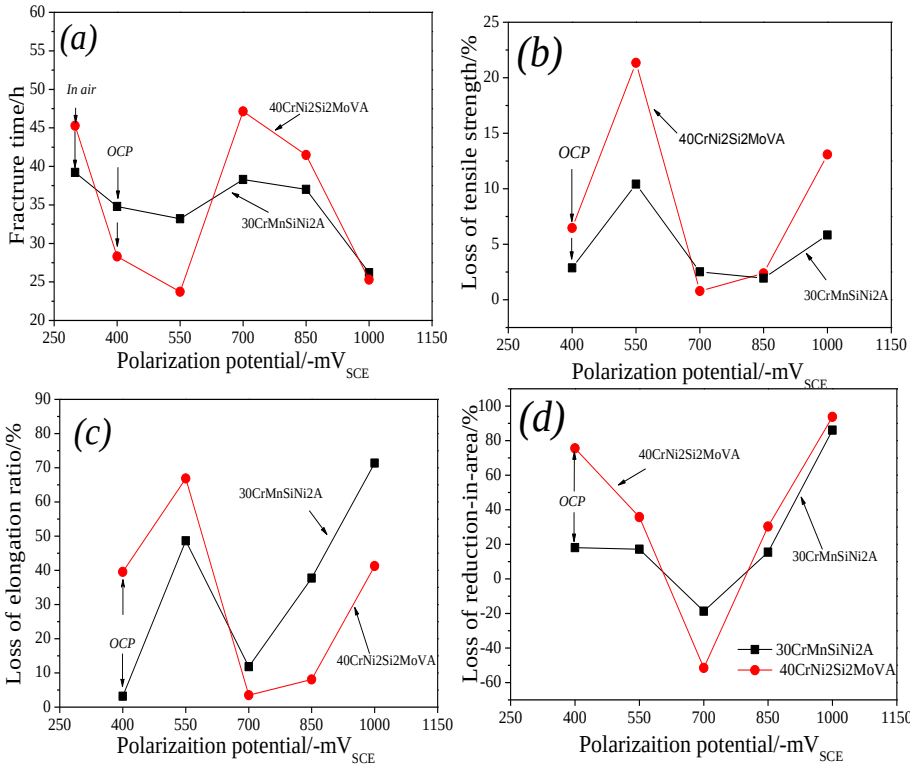

Figure 3. Fracture time (t_f) and tensile strength loss (I_σ), elongation loss (I_δ) and reduction-in-area loss (I_Ψ) of 30CrMnSiNi2A and 40CrNi2Si2MoVA at different polarization potentials in neutral 3.5wt% NaCl solution

Fig.3 (a-d) show fracture time (t_f) and tensile strength loss (I_σ), elongation loss (I_δ) and reduction-in-area loss (I_Ψ) at different applied potentials, respectively. For 30CrMnSiNi2A, t_f is the shortest at –1000 mV_{SCE} in all applied potentials, secondly at –550 mV_{SCE}, and then at OCP; however, t_f at –850 and –700 mV_{SCE} is longer than that at OCP. For 40CrNi2Si2MoVA, t_f is the shortest at –550 mV_{SCE}, secondly at –1000 mV_{SCE} and then at OCP; t_f at –700 and –850 mV_{SCE} is much longer than that of OCP. Moreover, t_f at –700 mV_{SCE} is the longest in all polarization potential, even more than that in air.

As shown in Fig.3 (b), for both 30CrMnSiNi2A and 40CrNi2Si2MoVA, I_σ at –550 mV_{SCE} is the highest in all applied potentials, respectively, secondly at –1000 mV_{SCE}; however, I_σ at –700

mV_{SCE} is the lowest. I_σ at –700 and –850 mV_{SCE} of 30CrMnSiNi2A shows more than that at OCP. Moreover, I_σ of 40CrNi2Si2MoVA at –700 and –850 mV_{SCE} is much higher than that at OCP.

In Fig.3 (c), I_δ at OCP and –700 mV_{SCE} of 30CrMnSiNi2A is lower than those at other potentials; the value at –1000 mV_{SCE} shows the highest value. I_δ at –700 and –850 mV_{SCE} of 40CrNi2Si2MoVA is lower than others. I_δ at –550 mV_{SCE} of 40CrNi2Si2MoVA shows the highest value in all the applied potentials. I_δ at OCP and –1000 mV_{SCE} of 40CrNi2Si2MoVA approached to each other. However, the value of I_δ at –850 and –1000 mV_{SCE} of 30CrMnSiNi2A is much higher than those of 40CrNi2Si2MoVA.

In Fig.3 (d), I_Ψ of 30CrMnSiNi2A and 40CrNi2Si2MoVA shows negative value at –700 mV_{SCE}, which increases with applied potentials increasing or decreasing from –700 mV_{SCE}. The value of I_Ψ of 40CrNi2Si2MoVA at OCP is much than that of 30CrMnSiNi2A at OCP. The values of I_Ψ of 40CrNi2Si2MoVA at –850, –1000 mV_{SCE} is close with those of 30CrMnSiNi2A, respectively.

In all, 40CrNi2Si2MoVA shows much higher SCC susceptibility than 30CrMnSiNi2A at OCP and –550 mV_{SCE}. 40CrNi2Si2MoVA and 30CrMnSiNi2A both display the similar SCC susceptibility at –1000 mV_{SCE}.

3.2 Fractography

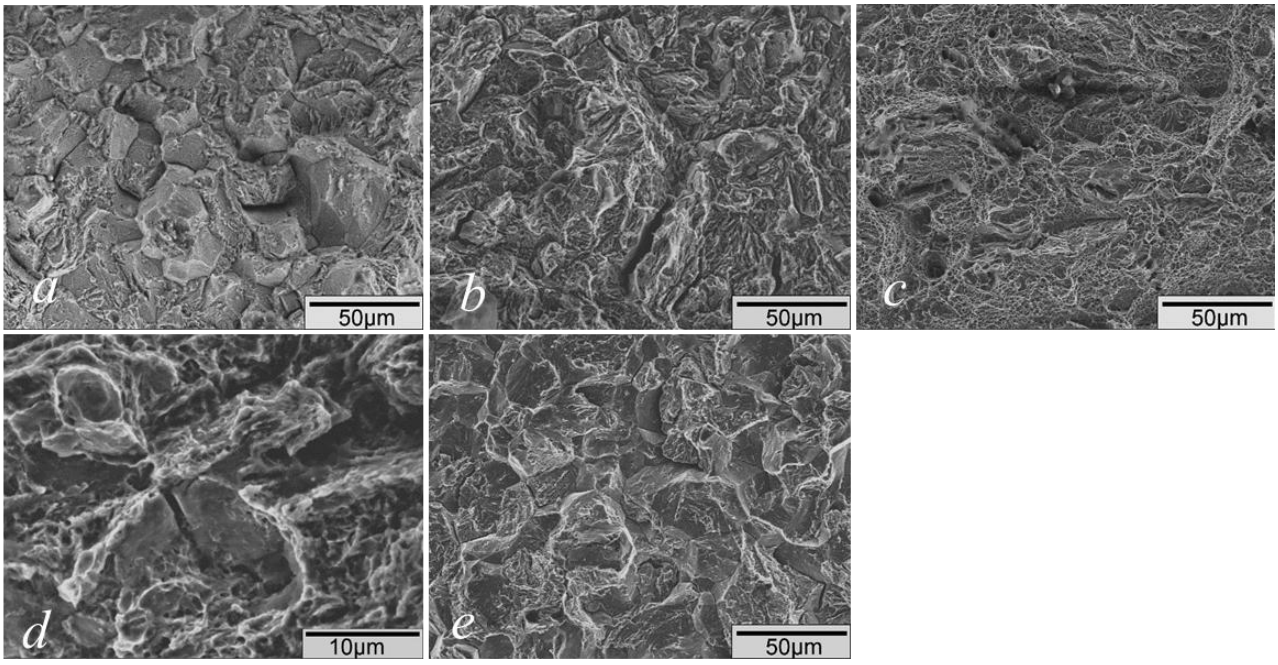

Figure 4. Fracture morphology of the SSRT 30CrMnSiNi2A specimens applied at different potentials (a-e: OCP; –550 mV_{SCE}; –700 mV_{SCE}; –850 mV_{SCE}; –1000 mV_{SCE})

Fig.4 (a-e) shows that the fracture morphology of 30CrMnSiNi2A at different applied potentials. At OCP and –1000 mV_{SCE} of 30CrMnSiNi2A, the brittle fracture surface is composed of intergranular fracture and secondary cracks; at –700mV_{SCE}, there are little cleavage regions and dimples in the fracture; at –850 mV_{SCE}, there are several small brittle facture in a small area distributed

along edge, mainly composed of intergranular fracture and secondary cracks. At –550 mV_{SCE}, there are intergranular fracture characteristic and some secondary cracks with obvious corrosion mark in the brittle fracture.

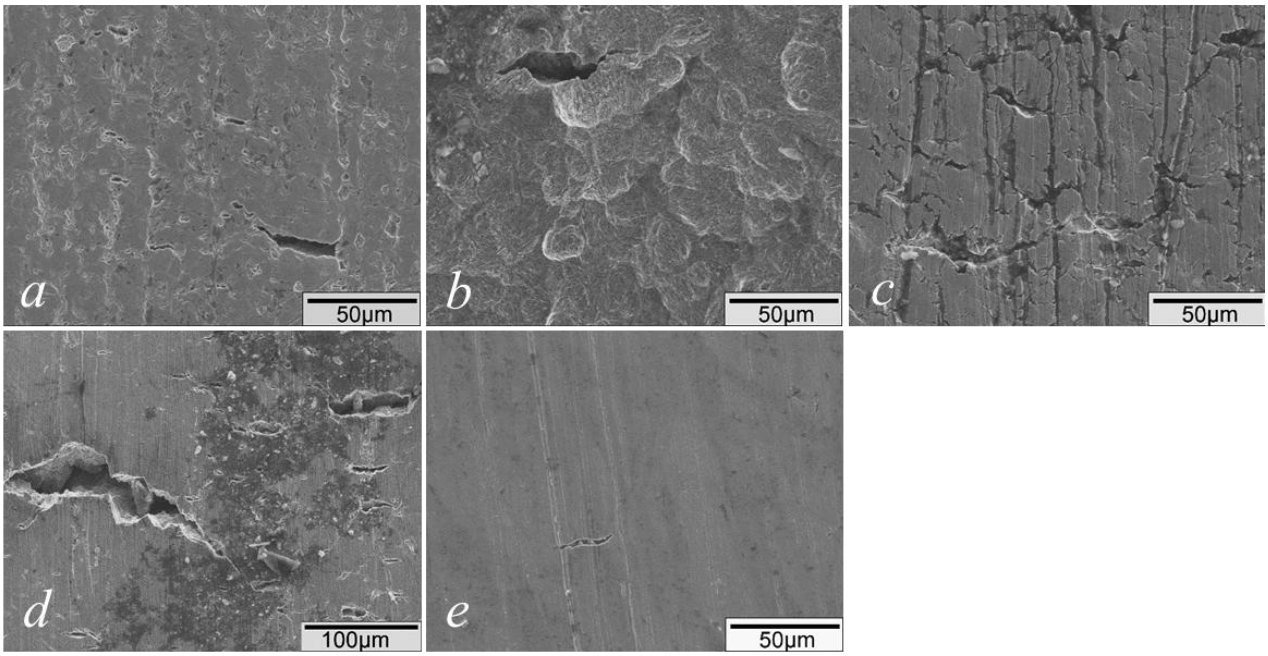

Figure 5. Side surface morphology close to the fracture of the SSRT 30CrMnSiNi2A specimens applied at different potentials (a-e: OCP; –550 mV_{SCE}; –700 mV_{SCE}; –850 mV_{SCE}; –1000 mV_{SCE})

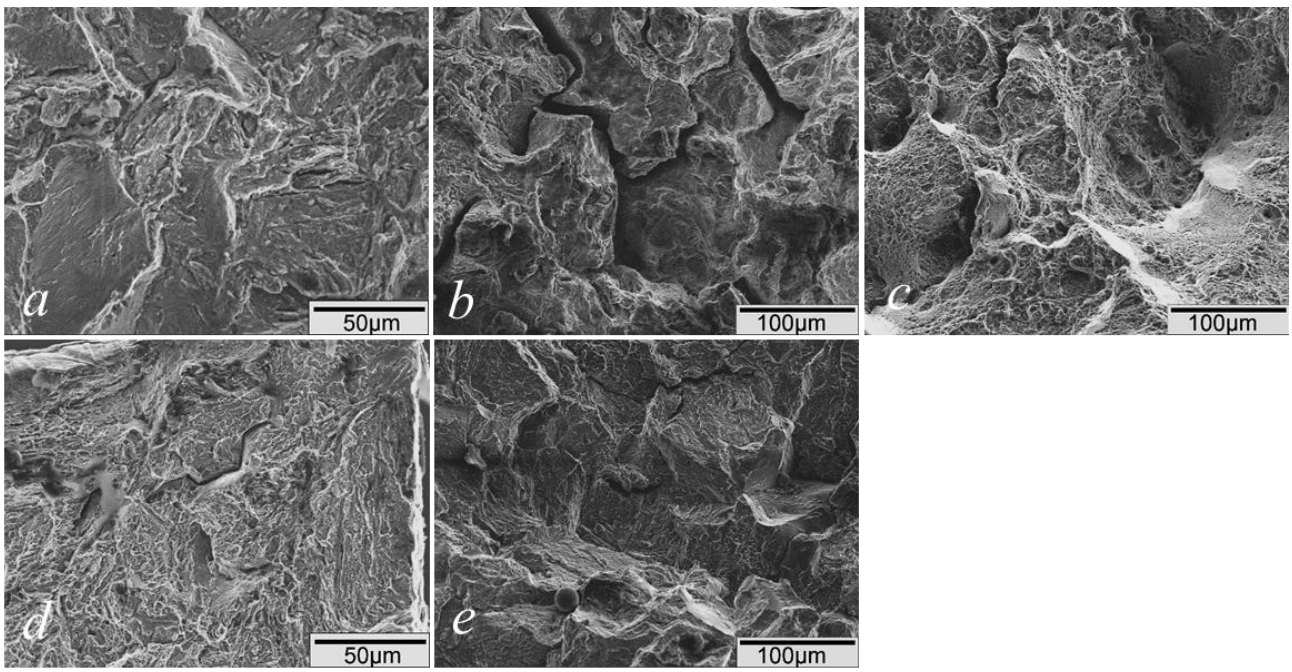

Figure 6. Fracture morphology of the SSRT 40CrNi2Si2MoVA specimens applied at different potentials (a-e: OCP; –550 mV_{SCE}; –700 mV_{SCE}; –850 mV_{SCE}; –1000 mV_{SCE})

Fig.5 (a-e) shows that the side morphology close to fracture of 30CrMnSiNi2A at different applied potentials. In side morphology, there are a few cracks and corrosion pits on the side surface at OCP. A lot of pits and minor broad cracks are present on the side surface at –550 mV_{SCE}. At –700 mV_{SCE}, a lot of shallow cracks on the surface of the steel is initiated; at -850 mV_{SCE}, more secondary cracks appear on the surface of the steel without any pits. At –1000 mV_{SCE}, minor secondary cracks are found on the side surface.

Fig.6 (a-e) exhibits the fracture morphology of the SSRT 40CrNi2Si2MoVA specimens applied at different potentials. At OCP, fracture surface of 300M is composed of intergranular, transgranular and secondary cracks fracture mode. At –550 mV_{SCE}, there are mainly cleavage facets, with corrosion mark in the fracture, which shows characteristics of anodic dissolution. At –700 mV_{SCE}, the fracture surface consists of quasi-cleavage and cleavage region. At –850 mV_{SCE}, the brittle area is very small, and mainly contains quasi-cleavage and secondary cracks. At –1000 mV_{SCE}, the brittle area is very broad, and mainly consists of cleavage and intergranular fracture modes.

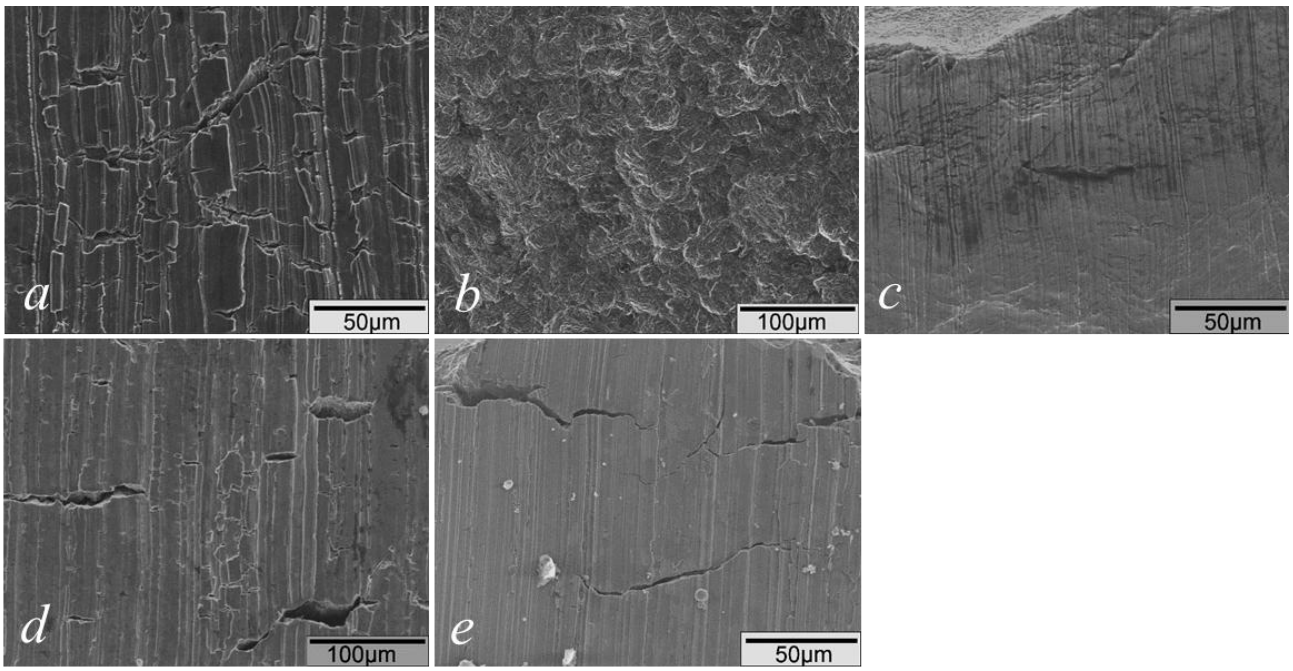

Figure 7. The side surface morphology close to the fracture of the SSRT 40CrNi2Si2MoVA specimens applied at different potentials (a-e: OCP; –550 mV_{SCE}; –700 mV_{SCE}; –850 mV_{SCE}; –1000 mV_{SCE})

Fig.7 (a-e) shows side surface morphology close to fracture of the SSRT 40CrNi2Si2MoVA specimens applied at different potentials. At OCP, the side surface of 40CrNi2Si2MoVA shows fragmented cracks and corrosion marks. At –550 mV_{SCE}, the side surface of the steel is seriously corroded with many shallow pits. The side surface at –700 mV_{SCE} shows remarkable deformation morphology with little cracks. At –850mV, there are a few broad cracks and a lot of small cracks. At –1000 mV_{SCE}, there are only few long secondary cracks in the side surface beneath the fracture.

3.3 Potentiodynamic polarization curves

Fig.8 (a-b) show potentiodynamic polarization curves of 30CrMnSiNi2A and 40CrNi2Si2MoVA with low and fast sweep rates of 0.5 and 50 mV/s, respectively. Corrosion potential (E_{corr}), corrosion current density (I_{corr}), anodic slope (β_a) and cathodic slope (βc) of 30CrMnSiNi2A and 40CrNi2Si2MoVA at a sweep rate of 0.5 mV/s are shown in Tab.2. At 50 mV/s, the corrosion potentials of 30CrMnSiNi2A and 40CrNi2Si2MoVA are –900 and –975 mV_{SCE}, respectively. In Fig.8 (a) and (b), they show no passivity of the steels with different sweep rates in neutral 3.5 wt% NaCl solution.

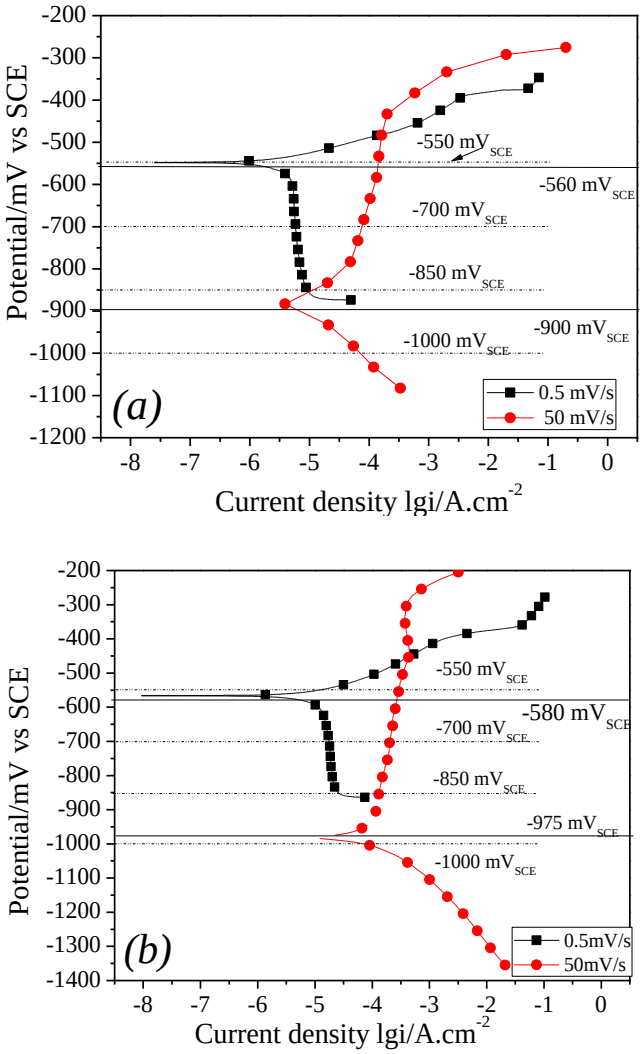

Figure 8. Potentiodynamic polarization curves of 30CrMnSiNi2A (a) and 40CrNi2Si2MoVA (b) with fast and slow sweep rates 50 and 0.5 mV/s in neutral 3.5 wt% NaCl solution

Table 2. The corrosion potential (E_{corr}), corrosion current density (I_{corr}), anodic slope (β_a) and cathodic slope (βc) of 30CrMnSiNi2A and 40CrNi2Si2MoVA at a sweep rate of 0.5 mV/s

	E_{corr} /mV_{SCE}	I_{corr} /$mA.cm^{-2}$	β_a / $mV.decade^{-1}$	β_c / $mV.decade^{-1}$
30CrMnSiNi2A	–560	0.0046	48.85	434.78
40CrNi2Si2MoVA	–580	0.014	84.21	750

4. DISCUSSION

The potentiodynamic polarization measurements of the steels 30CrMnSiNi2A and 40CrNi2Si2MoVA with different sweep rates of 0.5 and 50 mV/s confirms that the steels show little occurrence of spontaneous passivation in neutral 3.5 wt% NaCl solution. Due to lower content of Cr, 40CrNi2Si2MoVA shows lower corrosion resistance than 30CrMnSiNi2A in the initial periods, according to the results of E_{corr}, I_{corr}, β_a and β_c in Tab.2. According to Park's work [21-22], during slow sweeping, there is sufficient time for the formation of rust on the steel surface, which could be used to simulate the quasi-stable electrochemistry of the crack wall. With sweep rate increasing, the quasi-equilibrium state was disturbed and changed into non-equilibrium condition. At fast sweeping, the rust formation is inhibited, which generates a potential range where the steel is under active dissolution state to simulate the crack tip electrochemistry.

According to the corrosion potentials obtained from Fig.8, the potentiodynamic polarization curves of 30CrMnSiNi2A and 40CrNi2Si2MoVA with fast and slow sweep rates of 0.5 and 50 mV/s were separated into different potential regions, as shown in Fig.8 (a) and (b). To be clearly discussed, the applied potentials were also marked in the polarization curves in Fig.8 (a) and (b), respectively.

For 30CrMnSiNi2A, the polarization curves could be divided into three sections for the discussion of SCC mechanism, such as region I: $E \geq -560\ mV_{SCE}$, the crack tip and crack wall are both in anodic polarization state; region II: $-900\ mV_{SCE} < E < -560\ mV_{SCE}$, the crack tip and crack wall are in anodic and cathodic polarization, respectively; region III: $E \leq -900\ mV_{SCE}$, the crack tip and crack wall are both in cathodic polarization state.

In region I, i.e. at $-550\ mV_{SCE}$, 30CrMnSiNi2A shows excellent ductile characteristic, such as low elongation loss. It confirms that the steel shows excellent SCC resistance at anodic polarization. The high reduction-in-area loss of the steel at $-550\ mV_{SCE}$ is due to serious electrochemical dissolution.

In region II, i.e. at -700 and $-850\ mV_{SCE}$, the crack tip and crack wall of 30CrMnSiNi2A stay in anodic dissolution and cathodic polarization mode, respectively. The hydrogen evolution potential in neutral NaCl solution occurs at $-584.7\ mV_{SCE}$, which is calculated according to Eq. (4) [23-24]. With polarization potential decreasing, the hydrogen evolution increases. The elongation loss and reduction-in-area loss increases with polarization potential increasing.

$$E_H(mV_{SCE}) = -59 \times pH - 177.6 \quad (4)$$

In region III, i.e. at $-1000\ mV_{SCE}$, the reduction of hydrogen at the crack tip and crack wall plays as dominant cathodic reaction. The hydrogen atoms in the steel reaches the critical amount responsible for HIC. At the condition, the SCC behaviour is prohibited, and in fact, hydrogen embrittlement is responsible for the failure of the steel at the polarization potential. 30CrMnSiNi2A shows high susceptibility to hydrogen embrittlement at $-1000\ mV_{SCE}$.

$$H_2O + e \rightarrow H + OH^- \quad (5)$$

At OCP, 30CrMnSiNi2A shows good mechanical properties, such as low values of fracture strength loss, elongation loss and reduction-in-area loss. It means that the steel has excellent SCC resistance in neutral 3.5wt% NaCl solution. The fracture mode of 30CrMnSiNi2A at OCP shows

intergranular and transgranular fracture morphology. Therefore, the SCC mechanism of 30CrMnSiNi2A is mainly under control of HIC.

For 40CrNi2Si2MoVA, region I: E≥ –580 mV_{SCE}, the crack tip and wall is in anodic polarization; region II: –975 mV_{SCE} <E< –580 mV_{SCE}, the crack tip is in anodic dissolution state and the crack wall is in cathodic polarization status; region III: E≤ –975 mV_{SCE}, the crack tip and crack wall are both in cathodic polarization state.

In region I, i.e. at –550 mV_{SCE}, anodic dissolution of the steel both occurs at crack tip and wall. The steel shows low fracture strength and much higher values of reduction-in-area loss and elongation loss than 30CrMnSiNi2A at –550 mV_{SCE}. It indicates that the steel shows high susceptibility to SCC induced by anodic dissolution.

In region II, such as, at –700, –850 mV_{SCE}, the crack wall is in cathodic polarization state and the crack tip is under anodic dissolution mode. The effect of HIC on the SCC behaviour increases and the effect of anodic dissolution decreases with polarization potential decreasing from –700 to –850 mV_{SCE}.

In region III, i.e. at –1000 mV_{SCE}, as polarization potential decreases to –1000 mV_{SCE}, hydrogen evaluation plays dominant cathodic reaction (Eq. 5), and the hydrogen evolution increases to a critical amount for hydrogen embrittlement. It results in a large ductile loss at the polarization potential. 40CrNi2Si2MoVA shows higher ductile loss than 30CrMnSiNi2A at –1000 mV_{SCE}, such as fracture strength loss and reduction-in-area loss. It indicates that 40CrNi2Si2MoVA is more susceptible to hydrogen embrittlement than 30CrMnSiNi2A.

At OCP, 40CrNi2Si2MoVA shows high value of ductility loss. 40CrNi2Si2MoVA shows much more susceptibility to SCC behaviour than 30CrMnSiNi2A at OCP. Due to high SCC susceptibility induced by anodic dissolution of 40CrNi2Si2MoVA, the SCC mechanism at OCP is mainly controlled by a mixed mode of anodic dissolution and HIC.

5. CONCLUSIONS

(1) At anodic polarization potential –550 mV_{SCE}, the low alloy ultra-high strength steel 30CrMnSiNi2A shows excellent resistance to SCC. At cathodic polarization –1000 mV_{SCE}, the steel shows high susceptibility to SCC induced by HIC. The SCC mechanism at OCP is mainly controlled by HIC.

(2) At anodic polarization potential –550 mV_{SCE}, 40CrNi2Si2MoVA shows high susceptibility to SCC, which is controlled by anodic dissolution. At –1000 mV_{SCE}, the steel shows high susceptibility of SCC behaviour. The SCC mechanism at OCP is under control of a mixed mode of anodic dissolution and HIC, which shows higher SCC susceptibility than 30CrMnSiNi2A.

ACKNOWLEDGEMENTS
This work was supported by the National Natural Science Foundation of China (Grant No.51171011).

References

1. B.Y. Fang, A. Atrens, J.Q. Wang, E.H. Han, Z.Y. Zhu, W. Ke, *J. Mater. Sci.*, 38(2003) 127.
2. C. Liu, D.D. Macdonald, *J. Press. Vess. Technol.*, 119(1997) 393.

3. W.G. Hou, W.F. Zhang, Z.R. Wang, M.L. Ding, *Chinese J. Aeronaut.*, 24(2011) 527.
4. N. Winzer, A. Atrens, G. Song, E. Ghali, W. Dietzel, K.U. Kainer, N. Hort, C. Blawert, *Adv. Eng. Mater.*, 7(2005) 659.
5. W.Y. Maeng, H.H. Lee, U.C. Kim, *Corros. Sci.*, 47 (2005) 1876.
6. Lin Fan, Cuiwei Du, Zhiyong Liu, Xiaogang Li, *Int. J. Min. Met. Mater.*, 20(2013) 645.
7. C. Fahir Arisoy, Gokhan Basman, M. Kelami Sesen, *Eng. Fail. Anal.*, 10(2003) 711.
8. Z.Y. Liu, X.G. Li, C. W. Du, G.L. Zhai, Y.F. Cheng, *Corros. Sci.*, 50 (2008) 2251.
9. Y. Prawoto, A. Moin, M. Tadjuddin, W. B. Wan Nik, *Eng. Fail. Anal.*, 18 (2011) 1858.
10. A. Contreras, A. Albiter, M. Salazar, R. Pérez, *Mater. Sci. Eng. A*, 407 (2005) 45.
11. S. Ramannurthy, A, Atrens, *Corros. Sci.*, 52 (2010) 1042.
12. F. Sarıoglu, *Mater. Sci. Eng. A*, 315(2001) 98.
13. W.J. Hui, H. Dong, Y.Q. Weng, J. Shi, X.Z. Zhang, *Acta Metallur. Sin.*, 40 (2004) 1274.(In Chinese)
14. W.Y. Chu, S.Q. Li, C.M. Hsiao, S.Y. Ju, *Corrosion*, 37(1981) 514.
15. W.Y. Chu, S.Q. Li, C.M. Haiao, J.H. Tien, *Corrosion*, 36(1980) 475.
16. G. Wang, Y. Yan, J.X. Li, J.Y. Huang, Y.J. Su, L.J. Qiao, *Corros. Sci.* 77 (2013) 273.
17. F.R. Chen, L.X. Huo, Y.F.Zhang, I. Zhang, F.J. Liu, G. Chen, *J. Mater. Process. Tech.*, 129 (2012) 412.
18. F.G. Liu, X. Lin, M.H. Song, H.O. Yang, Y.Y. Zhang, L.L. Wang, W.D. Huang, J. Alloy Compd., 621(2015) 35.
19. J.Y. Zhong, M. Sun, D.B. Liu, X.G. Li, T.Q. Liu, *Int. J. Min. Met. Mater.*, 17(2010) 282.
20. D. Figueroa, M. J. Robinson, *Corros. Sci.*, 52(2010) 1593.
21. R.N. Parkins, *Corros. Sci.*, 20(1980) 147.
22. R.N. Parkins, *Corrosion*, 52(1996) 363.
23. A.Q. Fu, Y.F. Cheng, *Corros. Sci.*, 52(2010) 2511.
24. R.W. Revie, H.H. Uhlig, Corrosion and corrosion control, Fourth ed., Wiley, Hoboken, New jersey, 2008.